Title

Nanocellulose aerogel-based porous coaxial fibers for thermal insulation

Authors

Zhou, J

Hsieh, YL

Publication Date

2020-02-01

DOI

10.1016/j.nanoen.2019.104305

Peer reviewed

Nano Energy 68 (2020) 104305

Contents lists available at ScienceDirect

Nano Energy

journal homepage: http://www.elsevier.com/locate/nanoen

Nanocellulose aerogel-based porous coaxial fibers for thermal insulation

Jian Zhou, You-Lo Hsieh *

Fiber and Polymer Science, University of California, Davis, CA, 95616, United States

ARTICLE INFO

Keywords:
Nanocellulose
Aerogel
Porous fiber
Insulation
Thermal conductivity

ABSTRACT

Strong, continuous, and highly porous coaxial fibers with cellulose nanofibril (CNF) aerogel core and cellulose-rich sheath were fabricated by wet-spinning hollow fibers and infusing them with aerogel precursor for high-performance thermal insulators. The sheath contained multiscale pores, including microvoids (14.5 μm) and sub-micron pores (133 nm) in bulk, as well as ca. 25–26 nm surface nanopores, to function as a template and protective sheath for the microporous CNF aerogel core. The porous coaxial fibers had many desirable qualities, including low density (0.2 g cm^3), high porosity (85%), high specific tensile strength (23.5 ± 2.5 MPa g cm^{-3}), wide working temperatures (−20 to 150 °C), continuous and large-scale producibility, as well as biodegradability. The unique combination of multiscale porous sheath and ultra-low density aerogel core synergistically minimizes heat conductivity by all three mechanisms, i.e., restrain air circulation to limit convective heat transfer, while the poor conducting cellulose permitting little conductive heat transfer and the highly crystalline aerogel cellular walls prohibit infrared radiation, effectively suppresses radiative heat transfer under extreme temperatures.

1. Introduction

Aerogels are the least dense materials with densities approaching air and the most porous with porosity over 99%, thus are among the most unique for many potential applications, some yet to be discovered. While the most studied and commercially available aerogels are silica aerogels, significant interest has extended to others based on carbon, organic materials, metals and metal oxides [1–6]. However, aerogels are typically low tensile strength and Young's modulus, making them friable to be handled and used alone [7,8]. Being able to shape aerogels into desired forms and dimensions is attractive from the standpoint of integrating aerogels with other materials for strength and easy handle. In particular, incorporating three-dimensional (3D) aerogels into fibers or filaments are attractive from the standpoint of enabling fabrication into fibrous mats, woven, knitted and nonwoven fabrics, and flexible, stretchable or wearable materials, such as textiles, for thermal protective applications under either hot or cold extreme temperatures. However, high-performance aerogel fibers for insulation purpose are only explored to a very limited extent. Neat graphene aerogel fibers were wet-spun from aqueous liquid crystalline graphene oxide (GO) gels into liquid nitrogen to form aligned GO sheets with good mechanical strength [9]. However, coagulation in liquid nitrogen and fiber rigidity made continuous fiber production very challenging. Porous cellulose fibers with a diameter about 500 μm and 93–99% porosity were prepared by dissolving cotton linters in $Ca(SCN)_2$ or $ZnCl_2$ salt hydrate melt, then homogenized by a twin-screw extruder, and wet-spun into ethanol, finally dried in supercritical CO_2 [10]. The best fibers produced showed better heat resistance than cotton cloth under space flight conditions [11]. Both dissolution and coagulation are, however, chemically intensive, and the processes required to produce salt-free fibers are time-consuming. Moreover, densities of these porous fibers were not reported to be verified as aerogels.

We have fabricated aerogels using cellulose nanofibrils (CNFs) derived from rice straw cellulose through coupled TEMPO-mediated oxidation and mechanical defibrillation [12–17]. The rice straw derived CNFs are super fine (ca. 2 nm thick), six orders of magnitude smaller than porous rice straws (1.5 ± 0.5 mm wide) (Fig. 1a and b, and S1), and long (up to 1 μm) (Fig. 1c and d), thus having a very high aspect ratio and specific surface. Furthermore, these CNF surfaces are amphiphilic, allowing their self-assembling into unique aerogels of super low density (2–8 mg cm^{-3}), ultra-high porosity (>99.5%), high specific surface area (123 $m^2 g^{-1}$) with a 0.37 $cm^3 g^{-1}$ pore volume, and wet-resilience while retaining amphiphilicity [8,14,15,17–20]. Thermal insulation is among many of the diverse potential applications of these CNF aerogels. First, cellulose is among the least thermally conductive materials. The CNF aerogel cellular structure limits air circulation,

* Corresponding author.
E-mail address: ylhsieh@ucdavis.edu (Y.-L. Hsieh).

https://doi.org/10.1016/j.nanoen.2019.104305
Received 14 May 2019; Received in revised form 11 November 2019; Accepted 16 November 2019
Available online 20 November 2019

making it good convective inhibitor, while its low transparency to infrared radiation inhibits radiative transmission. Such distinguished thermal insulation potential of these CNF aerogels coupled with their unique resiliency and biological origin are particularly attractive for wearable thermal insulators. Therefore, shaping the 3D bulk aerogel into 1D fibers is envisioned to enable integrating CNF aerogels into such devices with scalable potential. Here we designed an approach to obtain continuous sheath-core coaxial fibers with highly porous aerogel core for high-performance insulators. The sheath functions as a processable template as well as a surface layer to protect the integrity of the aerogel structure from external forces or the environment.

2. Results and discussion

2.1. Coaxial aerogel fibers

Fig. 1e illustrates a coaxial wet-spinning and post-treatment process to produce a hollow fiber, or circular sheath, to be filled with aqueous CNF aerogel precursor. The spinning nozzle consists of coaxial inner and outer channels constructed with 23 and 17 gauge (G) needles, respectively. The hollow fiber was first wet-spun using a cellulose acetate (CA) dominant spin dope in dimethylacetamide (DMAc) for the outer channel and water for the center. A high molecular weight (4,000 kDa) poly (acrylic acid) (PAA) was added to CA at a 23:2 w/w CA/PAA ratio and spun into a water coagulation bath where the water inside and outside of the hollow fiber extracted DMAc, causing simultaneous phase inversion in the sheath and enabling continuous collection of single CA/PAA filament over 10 m long. The ease in which uniform fiber was spun continuously validated the potential for scaled-up production. The as-spun hollow fiber was immersed in water for an additional 15 h to remove residual DMAc while keeping the core filled with water. The water-filled hollow fiber was frozen (−20 °C, 15 h), then freeze-dried in a lyophilizer (−50 °C for 2 d) into a uniform hollow fiber template for infusion with aerogel precursor. Aqueous CNF dispersion (0.7 wt%) was then injected into the hollow fiber at 300 μl min^{-1} (Fig. S2a), followed by freezing (−20 °C, 15 h), then freeze-drying (−50 °C for 2 d) to form continuous aerogel in the core. Fig. 1f and g shows the final hollow CA/PAA fibers whereas the aerogel core was sufficiently strong to be pulled out from the hollow fiber (Fig. 1h and i). Moreover, the fabrication process is streamlined to allow continuous production of a large number of coaxial fibers (Fig. S2b). These hollow and coaxial fibers were relatively uniform in their lateral dimensions, as shown by their respective average outer diameter of 1010.9 ± 50.7 μm and 905.9 ± 38.0 μm on 30 locations along two representative fibers (Fig. S3).

The SEM of the hollow fiber cross-section showed an average outer diameter of 992.7 (±46.6) μm with an average wall thickness of 155.7 (±21.2) μm (Fig. 2 a-f). The wall is characterized by a double concentric layer of porous structures (Fig. 2a) from phase inversion caused by water exposure from both inside and outside of the hollow fiber during immersion precipitation and coagulation. The porous structures are thought to originate from the combination of phase separation and mass transfer among CA/PAA (polymer), DMAc (solvent), and water (coagulant) during phase inversion. The microvoids in the hollow fiber wall were several to tens of micrometers (average value: 14.5 ± 13.1 μm) in widths in both inner and outer layers (Fig. 2b and c). Further enlargements of the hollow fiber wall showed the additional porous morphology consisting of sub-micron pores with an average diameter of 133 (±49) nm (Fig. 2d) and even smaller nanopores on both inner (24.8 ± 5.2 nm) and outer (25.8 ± 5.0 nm) surfaces (Fig. 2e and f). Therefore, the sheath contains multiscale porous structure in three

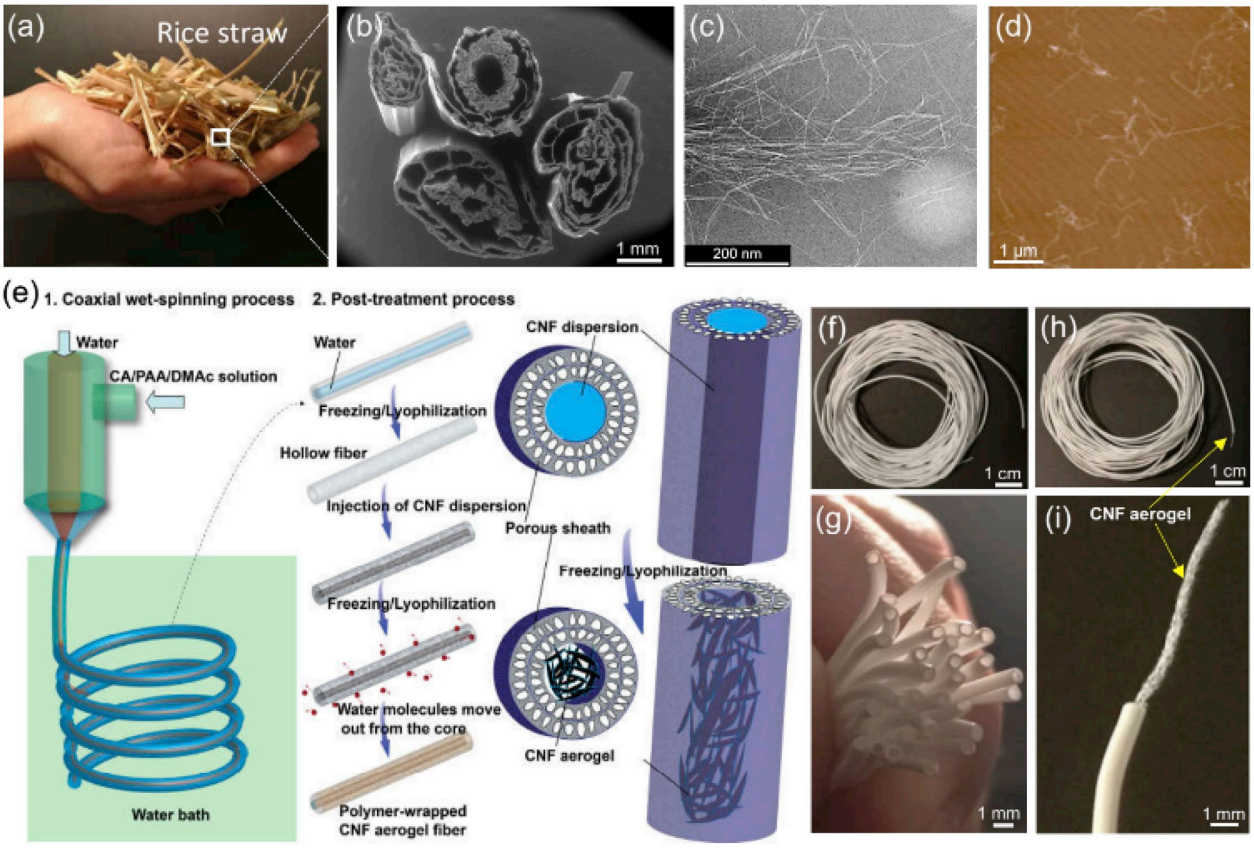

Fig. 1. Rice straw cellulose, nanocellulose and hollow and coaxial fibers. (a) Photograph of rice straws. (b) SEM image of typical rice straw cross-sections showing multilayer porous microstructures. (c, d) TEM and AFM images of CNFs derived from rice straw cellulose, respectively. (e) Schematic illustrations of coaxial wet-spinning of CA/PAA hollow fiber and post-processes to produce CNF aerogel core in coaxial fibers. (f, g) Photographs of CA/PAA hollow fibers. (h, i) The CA/PAA-sheath and CNF aerogel-core coaxial fibers with arrows pointing the exposed CNF aerogel core of one coaxial fiber.

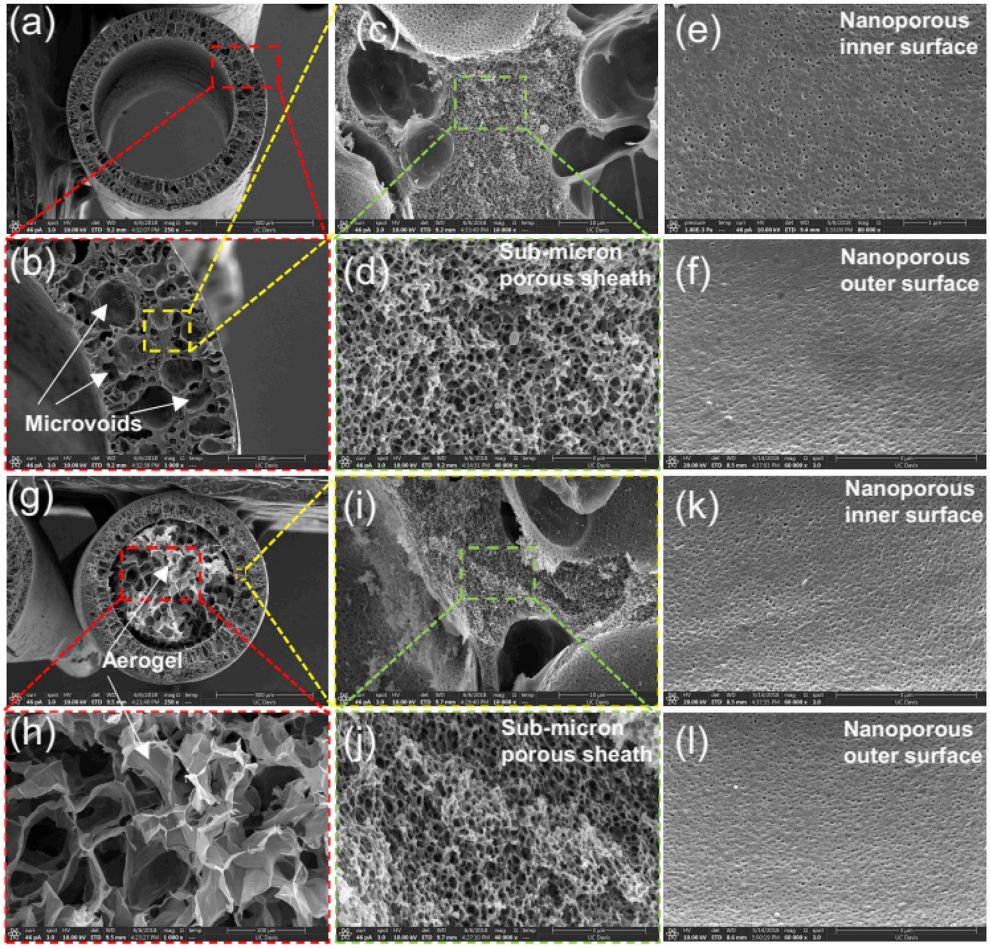

Fig. 2. Morphologies and microstructures of hollow and coaxial fibers by SEM. (a) The CA/PAA hollow fiber cross-section. (b–d) The enlarged hollow fiber sheath cross-sections are showing microvoids surrounded by sub-micron porous and nanoporous structure. (e, f) The inner and outer surfaces of the hollow fiber showing nanoporous structures. (g) The coaxial fiber cross-section is showing a porous sheath and a porous core. (h) The CNF aerogel core of the coaxial fiber. (i, j) The sheath in coaxial fiber showing similar microvoids surrounded by sub-micron and nanoporous structures as in hollow fiber sheath. (k, l) The inner and outer surfaces of the coaxial fiber sheath showing nanoporous structure.

orders of magnitude levels, i.e., tens of μm wide microvoids surrounded by numerous two order magnitude smaller sub-micron pores across the wall thickness and even smaller nanopores on both the inner and outer surfaces. This porous sheath is critical to mass transfer of water and ice sublimation during lyophilization from the core, enabling the formation of CNF aerogels in the core. The formation of hierarchical pores in the hollow fiber wall is attributed to DMAc-water liquid-liquid demixing and mass transfer in the overall phase separation process. The thin nanoporous inner and outer skins are thought to be formed with fast coagulation or instantaneous demixing with water inside and outside the hollow fibers. The densely packed skins limit solvent outflow to facilitate droplet nucleation and sub-micron pore formation in the sheath where the CA/PAA/DMAc mixture phase separate into a solvent-rich or polymer-lean phase and a polymer-rich phase to minimize the Gibbs free energy of mixing. The microvoids in the sheath are likely formed by two generally accepted mechanisms: (1) diffusion aided by the Marangoni effect, i.e., mass transfer along an interface between two fluids due to surface tension gradient; (2) local surface instability, skin rupture and solvent intrusion [21]. The sub-micron pores may originate from droplets of the solvent-rich phase that grows as a continuous entity as long as the solution beyond the droplet boundary is stable.

Following the injection of aq. CNF dispersion into the hollow fiber and the subsequent lyophilization, a coaxial microstructure with cellular CNF aerogel in the core and multiscale porous sheath is evident as shown in the cross-sectional SEM image in Fig. 2g-l. The coaxial fiber's outer diameter was 846.2 ± 18.6 μm with a wall thickness of 118.9 ± 14.9 μm, both smaller than the original hollow fiber and evident of shrinkage (Fig. 2a). While the outer diameter reduced by ca. 15%, the larger ca. 24% thinning of the wall resulted in ca. 13% reduction of inner core diameter, similar to the overall fiber width reduction. This consistent shrinkage of the core, wall thickness, and overall coaxial fiber dimension may be attributed to the compatibility between CNF in the core and CA-dominate sheath and their similar behaviors during freezing and lyophilization. The aerogel fully occupied the fiber core and appeared similar to neat aerogel, indicating neither ice nucleation nor lyophilization of the aq. CNF was affected by the sheath, a testament to its porous nature. The CNF aerogel is highly porous, containing 41.8 ± 24.1 μm average pores (Fig. 2g and h), nearly three times the microvoid sizes in the sheath. The double layer voids across the wall thickness range from several to tens of micrometers also remained unchanged. The average diameter of the nanopores in the sheath of the coaxial fiber was 138 ± 55 nm (Fig. 2i and j), comparable to that of the hollow fibers (133 ± 49 nm). Furthermore, the pores on the inner and outer surfaces of the coaxial fiber had an average diameter of 26 ± 5 nm and 25 ± 4 nm, respectively (Fig. 2k and l). Again, that the pore sizes of both sub-micron and nanopores in the sheath remain essentially unaltered with aerogel core gave evidence to their chemical similarity and compatibility.

The linear density measured from the mass of equal length (2.56 m) of the hollow fiber and coaxial fiber was 1.07 and 1.10 mg cm^{-1}, respectively, that were calculated into 0.48 and 0.2 g cm^{-3} overall bulk densities or 63 and 85% porosity, respectively. The density of the CNF aerogel core was calculated from the mass difference between the coaxial fiber and the hollow fiber of equal lengths and the diameter of the CNF core measured from Fig. 2g to be 8.5 mg cm^{-3}, comparable to that of neat CNF aerogel [15] and again confirming the CNF aerogel in the hollow fiber core to be unaffected by the sheath. Thus, the wet-spinning and post-injection of aq. CNF and lyophilization process (Fig. 1e) has

been validated for the fabrication of CA/PAA-sheath CNF aerogel core coaxial fibers. Most significantly, the cellulose derivative and high porosity of the hollow fiber sheath was vital to facilitate the successful formation of CNF aerogel core. Furthermore, this approach is versatile to produce different sizes of hollow fibers ($623.7 \pm 30.1\,\mu$m and $1297.6 \pm 80.4\,\mu$m) or coaxial fibers ($588.3 \pm 19.3\,\mu$m and $1191.4 \pm 60.6\,\mu$m) using different size of coaxial needles (Fig. S4).

Both hollow and coaxial fibers exhibited typical plastic deformation stress-strain curves under tensile loading (Fig. S5) and good flexibility with $6.6 \pm 1.2\%$ and $6.1 \pm 1.0\%$ elongation, respectively. Most significantly, the coaxial fibers had a specific mechanical strength of 23.5 ± 2.5 MPa g cm^{-3}, which is nearly twice as strong as the hollow fibers (12.3 ± 1.9 MPa g cm^{-3}). Moreover, the coaxial fibers also show a more than twice specific Young's Modulus of 987.0 ± 106.0 MPa g cm^{-3}, than that for hollow fibers (471.9 ± 70.8 MPa g cm^{-3}). The mechanical robustness of the coaxial fiber is impressive, clearly confirming the protective and strengthening the role of the sheath in expanding the tensile strength and flexibility of neat aerogel, making these coaxial fibers more processable and durable.

2.2. Thermal insulation

The thermal insulation behavior of the hollow and coaxial fibers under both hot and cold conditions was observed. In the first experiment, 10 fibers were packed tightly and aligned unidirectionally to form a single layer mat in ca. 1 mm thickness on a hotplate (Inset in Fig. 3a), and infrared images were taken during heating from 30 to 150 °C. The corresponding absolute temperature difference ($|\Delta T|$) of the fiber surface (T_f) and the hotplate were plotted against the hotplate temperature (T_h), with higher $|\Delta T|$ indicating better thermal insulation performance. Fig. 3a shows consistently higher $|\Delta T|$ of in 1-layer coaxial fiber mat than 1-layer hollow fiber mat at any given T_h. As T_h reached 150 °C, the coaxial fiber mat temperature increases to 125 °C as opposed to 130 °C with the hollow fiber mat, showing better thermal insulation properties of the coaxial fiber mat over that of the hollow fibers. With 2-layer fiber mat, the $|\Delta T|$ doubled for both types of fibers at the same T_h (Fig. 3c) and the higher increases in $|\Delta T|$ for double layers than single layers are due to the reduced thermal convection. At $T_h = 150$ °C, $|\Delta T|$ is 54 and 41 °C for coaxial and hollow fiber mat, respectively. The significantly better insulation performance of coaxial fibers than the hollow fibers is clearly attributed to the CNF aerogel in the core. Convective heat transfer in the hollow fibers is expected to be higher in the larger space within the

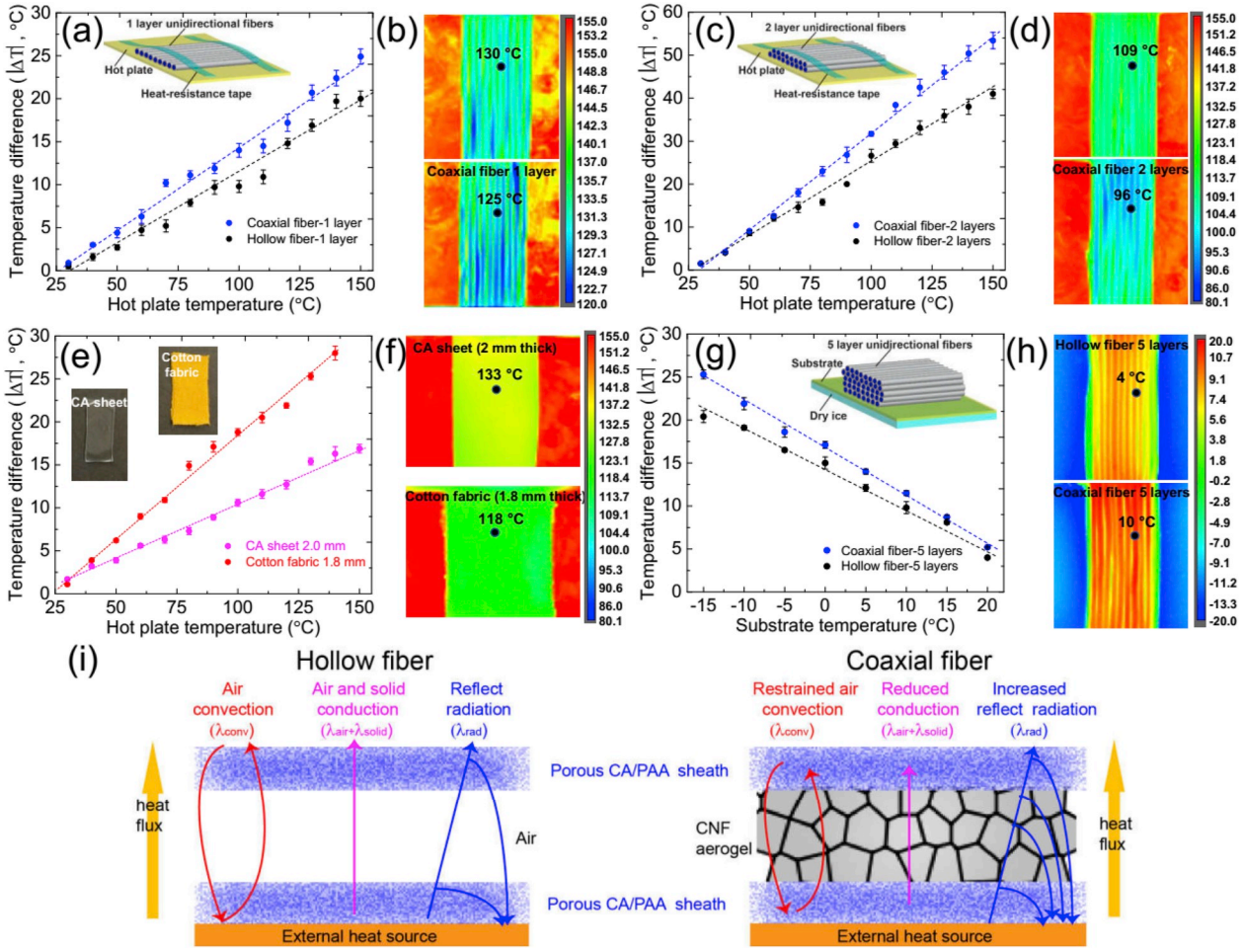

Fig. 3. Thermal insulation properties of the hollow and coaxial fiber mats. (a) Temperature difference ($|T|$) between the fiber surface (T_f) and hot plate (T_h) versus T_h for 1-layer hollow fibers and 1-layer coaxial fibers. Inset in (a) shows the temperature measurement setup. (b) The corresponding thermal images of 1-layer hollow fibers and 1-layer coaxial fibers at $T_h = 150$ °C. (c) Temperature difference ($|T|$) between T_f and T_h versus T_h for 2-layer hollow fibers and 2-layer coaxial fibers. Inset in (c) shows the temperature measurement setup. (d) Thermal images of 2-layer hollow fibers and 2-layer coaxial fibers at $T_h = 150$ °C. (e) Temperature difference ($|T|$) of the T_f and T_h versus the T_h for a 2 mm thick CA sheet and a 1.8 mm thick cotton fabric. Inset in (e) shows the optical images of a CA sheet and a cotton fabric. (f) The corresponding thermal images of the CA sheet and the cotton fabric at $T_h = 150$ °C. (g) Temperature difference ($|\Delta T|$) of the T_f and cold substrate (T_s) versus the T_s for 5-layer hollow fibers and 5-layer coaxial fibers. Inset in (a) shows the temperature measurement setup. (h) The corresponding thermal images of 5-layer hollow fibers and 5-layer coaxial fibers at $T_s = -15$ °C. (i) Schematic illustration of the thermal insulation mechanisms of the hollow and coaxial fibers.

hollow fiber (711.4 ± 23.3 μm) for fluid movement which, in contrast, would be suppressed in the much smaller pore sizes (41.8 ± 24.1 μm) in the CNF aerogel core, dramatically reducing and even ceasing convection among less connected pores. Moreover, the heat transfer by infrared radiation of the cellular wall in the CNF aerogel network was largely reduced in comparison to the air in the hollow fiber. The radiative thermal conductivity (λ_{rad}) in porous materials is given by Ref. [22]:

$$\lambda_{rad} = 16\sigma n^2 T^3/(3\rho K_s/\rho_s) \quad (1)$$

where σ is the Stephan-Boltzmann constant (5.67×10^{-8} W m^{-2} K^{-4}), n is the refractive index (~1 for aerogels), T is the mean temperature within the porous material, and Ks is the extinction coefficient for the solid material, ρ and ρ_s are the apparent and true density of the porous material, respectively. Based on this equation, λ_{rad} contributes exponentially more to the total thermal conductivity as temperature increases, as shown in Fig. 3c. Thus, by introducing aerogel in the core, the insulation performance of the coaxial fiber is superior to that of the hollow fiber, especially at higher temperatures.

Top surface temperature of 2-layer coaxial fiber mat with a thickness of 2 mm was measured to be 96 °C, considerably lower than 109 °C for the hollow fiber mat at $T_h = 150$ °C (Fig. 3c and d). The coaxial fiber mat also far out-performed two other cellulose materials of similar thickness: a single-layer transparent CA sheet cast from acetone (2 mm thick) and 3-layer cotton fabrics (1.8 mm thick) whose temperatures increase to 133 and 118 °C, respectively at $T_h = 150$ °C (Fig. 3e), and thermal images shown in Fig. 3f. While three layers of porous cotton fabrics display better insulation properties than the single sheet of non-porous transparent CA, cotton fabrics are less porous than hollow and coaxial fibers reported here, with 63% and 85% porosities, respectively. Comparing at the same $T_h = 80$ °C, the insulation performance ($|\Delta T| = 23$ °C) of the 2-layer coaxial fibers is also superior to that ($|\Delta T| = 18$ °C) of porous silk for bin fibers with aligned pores [23].

To simulate a cold environment, the 5-layer fiber mat was placed on top of a polystyrene substrate with a 3 cm thick slab of dry ice underneath (Inset in Fig. 3g). At −15 °C substrate temperature (T_s), the $|\Delta T|$ of the 5-layer coaxial fiber mat reduced to 10 °C, higher than 4 °C of the hollow fiber mat, again affirming excellent thermal insulation of coaxial fibers over hollow fibers in a cold environment. Therefore, layered coaxial fiber mats have demonstrated to be highly thermally insulating under both hot and cold external environment.

Fig. 3i shows the heat transfer mechanism of both hollow and coaxial fibers. The thermal conductivity of the hollow fibers, λ_{hollow} is expressed as

$$\lambda_{hollow} = \lambda_{conv1} + \lambda_{cond1} + \lambda_{rad1} \quad (2)$$

where λ_{conv1}, λ_{cond1}, and λ_{rad1} are is the respective heat transfer by convection, conduction, and radiation. The thermal conductivity of hollow fibers is drastically lower than solid fibers as air has much smaller thermal conductivity than solids. The multi-scale porous structure with a high 63% porosity in the hollow fiber sheath is critical in further reducing the overall heat transfer. First, the larger ca. 14.5 μm wide microvoids surrounded by well inter-connected sub-micron (ca. 133 nm) and ca. 25–26 nm nanopores significantly reduced thermal convection, λ_{conv1}, as air movement is seriously restricted within small porous network structures. Second, the sub-micron and 25–26 nm nanopore sizes are smaller than the 70 nm mean free path of gas molecules in the air. Finally, the reflected radiation (λ_{rad1}) of infrared light was significantly reduced due to the numerous solid-air interfaces in both sheath. These hierarchical porous structure serves multiple means to impede heat transfer and is evident when compared with the transparent CA cast sheet (the inset image in Fig. 3e). Common hollow fibers with nonporous sheath have been used alone or combined with solid fibers to achieve heat shielding and insulation by trapping air in the hollow core [24]. The multiscale pores in the sheath of the hollow fiber reported here offer additional advantages of being lighter, more porous and better thermally insulating than the ordinary hollow fibers, while also function as the processing template for aerogel formation in the core.

The thermal conductivity of the aerogel core ($\lambda_{aerogel}$) can be expressed by

$$\lambda_{aerogel} = \lambda_{cond2} + \lambda_{conv2} + \lambda_{rad2} \quad (3)$$

where λ_{cond2} is thermal conduction through the gas (air) and the solid (CNF) in the aerogel core. λ_{conv2} and λ_{rad2} are the heat transfer by convection and radiation of the aerogel, respectively.

The CNF aerogel core within hollow fiber further inhibits the thermal transfer mechanism in several ways. The large 10^1–10^2 μm cellular spacings in CNF aerogel inhibit convection by restraining air circulation in over 99.5% pore volume [14,15,17], while permitting heat transfer by the poor thermal conducting and irregularly connected cellular walls whose highly crystallinity prohibit infrared radiation effectively in comparison to the optically transparent polymer films or silica aerogels [8]. Clearly, the porous sheath of the hollow fiber surrounding the CNF aerogel core serves several crucial structural roles by providing the internal space and compatible surfaces for infilling aqueous CNF aerogel precursor; the mutliscale pore structure of the sheath allows water vapor diffusivity for aerogel formation; and the protective outer layer for handling. The multiscale porous structure in the sheath as well as in the ultra-porous aerogel core contribute synergistically in restraining thermal transfer by convection, conduction, and radiation.

Thermal conductivities of solid cellulose nanopaper made by vacuum filtration of nanocelluloses are 0.3–0.5 W (mK)$^{-1}$, irrespective of cellulose sources (including Tunicate, bacterial cellulose, cotton, and wood pulp) or nanocellulose preparation by sulfuric acid hydrolysis or TEMPO-mediated oxidation [25]. In contrast, the thermal conductivities of wood-derived CNF aerogels measured by transient hot-wire or temperature wave method were 0.018–0.06 W (mK)$^{-1}$, one order of magnitude lower than nanopaper due to their high porosity (>99%) [4a, 25,26]. It is obvious that the thermal conductivity depends on the density and the microstructure of the aerogels. As the pores in the aerogel core is tens of micrometer in widths (Fig. 2g and h), the thermal conductivity of the CNF aerogel here measured by a transient hot disk method was 0.04 W (mK)$^{-1}$, slightly higher than air.

Like most polymers, cellulose acetate (CA) solid has a thermal conductivity of 0.20 W (mK)$^{-1}$ [27]. The porous sheath of the CA hollow fibers gave lower measured thermal conductivity of 0.10 W (mK)$^{-1}$, attributing to its multiscale pores ranging from larger micropores (several to tens of μm or averaged 14.5 ± 13.1 μm) to the much smaller ca. 25 nm wide nanopores on both inner and outer surfaces that reduce overall heat transfer by convection and conduction, respectively. The aerogel core consists of large (10^1–10^2 μm) cellular spacings that significantly reduce convection. Couple the effective radiative heat barrier of both CA and CNF solids and the high sheath and core porosities, both the CNF aerogel core and CA-rich sheath contribute to the very low 0.07 W (mK)$^{-1}$ thermal conductivity of the coaxial fibers. While this measured thermal conductivity is higher than previously reported biobased aeropectin bulk aerogel and aeroSF fibers [23,28], the tensile strength of 4.7 MPa tensile strain of 6.1% of this coaxial aerogel fiber are far superior than silk aerogel AeroSF fiber with a reported 0.95 MPa tensile strength of and 0.08% breaking strain [23].

Clearly, the superior thermal insulation property of coaxial fibers (λ_{fiber}) is attributed to the synergistic thermal insulation characteristics of both the porous sheath and the aerogel core. In theory, the thermal insulation of such coaxial fibers may be further improved by engineering the microstructure in both core and sheath. For instance, reducing the pore sizes in the sheath to below the 70 nm mean free path of air, closing the opened cellular network into enclosed air pockets, or reducing the pore size of the aerogel core could potentially improve the conductive insulation of the coaxial fibers, while maintaining similar porosity. However, the volume ratio of the aerogel core and sheath may also need to be tuned to balance density, porosity, as well as thermal insulation

performance for specific need.

The effect of coaxial fiber layers on the insulation performance was conducted over a hotplate heated from 30 to 150 °C, with typical images shown in Fig. 4a, b, and c at $T_h = 50$, 100, and 150 °C, respectively. For the 5-layers coaxial fiber mat, the T_f was as low as 34, 57, and 81 °C, corresponding to $|\Delta T|$ of 16, 43, and 69 °C at $T_h = 50$, 100, and 150 °C, respectively. It is obvious that the greater numbers of layers, the lower the rate of heat transfer. By increasing the thickness of the coaxial fiber mat through which heat is transferred, as well as trapping pockets of air between the individual layers offer better thermal insulation. Thus, any targeted insulation performance of contact surfaces can be tuned by simply varying the thickness of the coaxial fiber mat or changing the numbers of the mat layers. Additional variation may include using different fiber diameters and sheath-core proportions to meet specific needs.

2.3. Demonstration of the fiber insulators

To further proof the concept on the thermal insulation performance of coaxial fibers under hot and cold environment, a larger aera 2-layer of coaxial fiber mat (dimension: 16 cm × 11 cm × 0.2 cm) was made by packing 150 of 16 cm-length fibers unidirectionally as the base layer, then overlay parallelly another layer of 150 fibers, as shown in Fig. 5a, b and S6. Then a toy house (dimension: 16 cm × 11.5 cm × 13 cm) was constructed and the fiber m 5c). The front wall of the house was left open to observe temperature distribution inside using a thermal camera. Summer heat was simulated by lighting a 100 W bulb 1 cm away from the top of the roof (Fig. 5d–f). After 20 min of irradiation from the bulb, the thermal image shows significantly lower temperature distribution in the house with coaxial fiber mat on the roof than that without (Fig. 5e and f). On the other hand, Winter cold was simulated by placing dry ice (in an aluminum tray) on the top of the roof (Fig. 5g–i). After 20 min of cooling by the dry ice, the house with coaxial fiber mat on the roof remained warmer than that without coaxial fibers (Fig. 5h and i). The temperatures at various locations in the house represented by "Picture", "Flower", and "Cat" marked as white dots in Fig. 5d and g were plotted over time in Fig. 5g-l. Upon heating, the internal temperatures in the house with coaxial fiber mats on the roof rose nearly linearly within the first 7–12 min, then levelled to 20 min, but were 6.2, 10.4 and 6.5 °C lower at "Picture", "Flower", and "Cat" locations, respectively (Fig. 5j-l). Upon cooling, temperatures in the house with coaxial fiber mats on the roof dropped at a higher rate within the first 5–10 min, then slowly lowered to 5.2, 4.8 and 4.0 °C higher at same "Picture", "Flower", and "Cat" locations, respectively (Fig. 5m–o). These simulations show the effectiveness of the coaxial fiber mat as thermal insulation for an enclosure or space to resists the heat gain in a hot environment and to heat loss in a cold environment. One can imagine that the temperature in the room can be tuned to a comfort zone by using different layers or diameter of coaxial fibers (Fig. 4). Moreover, this spatial thermal insulation application of the coaxial fibers is feasible in a wide range of

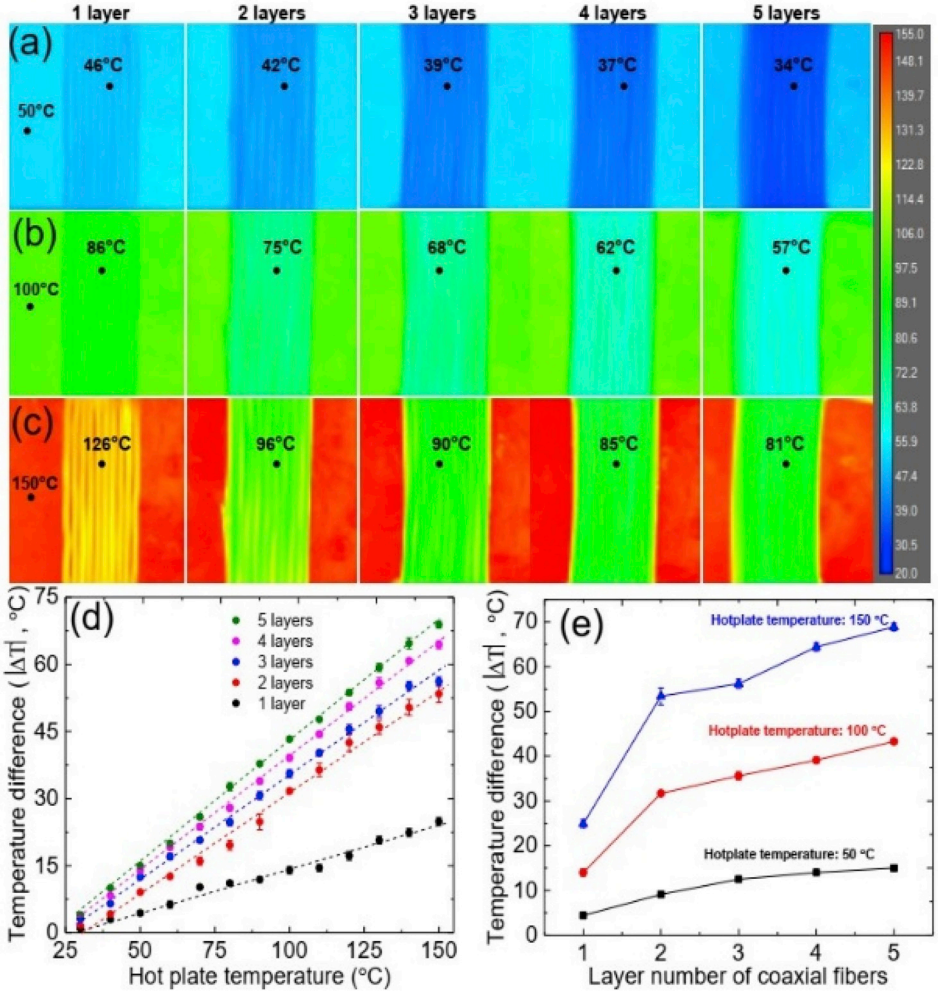

Fig. 4. Thermal insulation properties of coaxial fiber mats with different layers. (a–c) The thermal images of coaxial fiber mats with different layers at $T_h = 50$, 100, and 150 °C, respectively. (d) The temperature difference ($|T|$) between the fiber surface and hot plate versus the hotplate temperature for different layers of coaxial fibers. (e) The temperature difference ($|T|$) between the fiber surface and hot plate is plotted against layer number of the coaxial fiber mat.

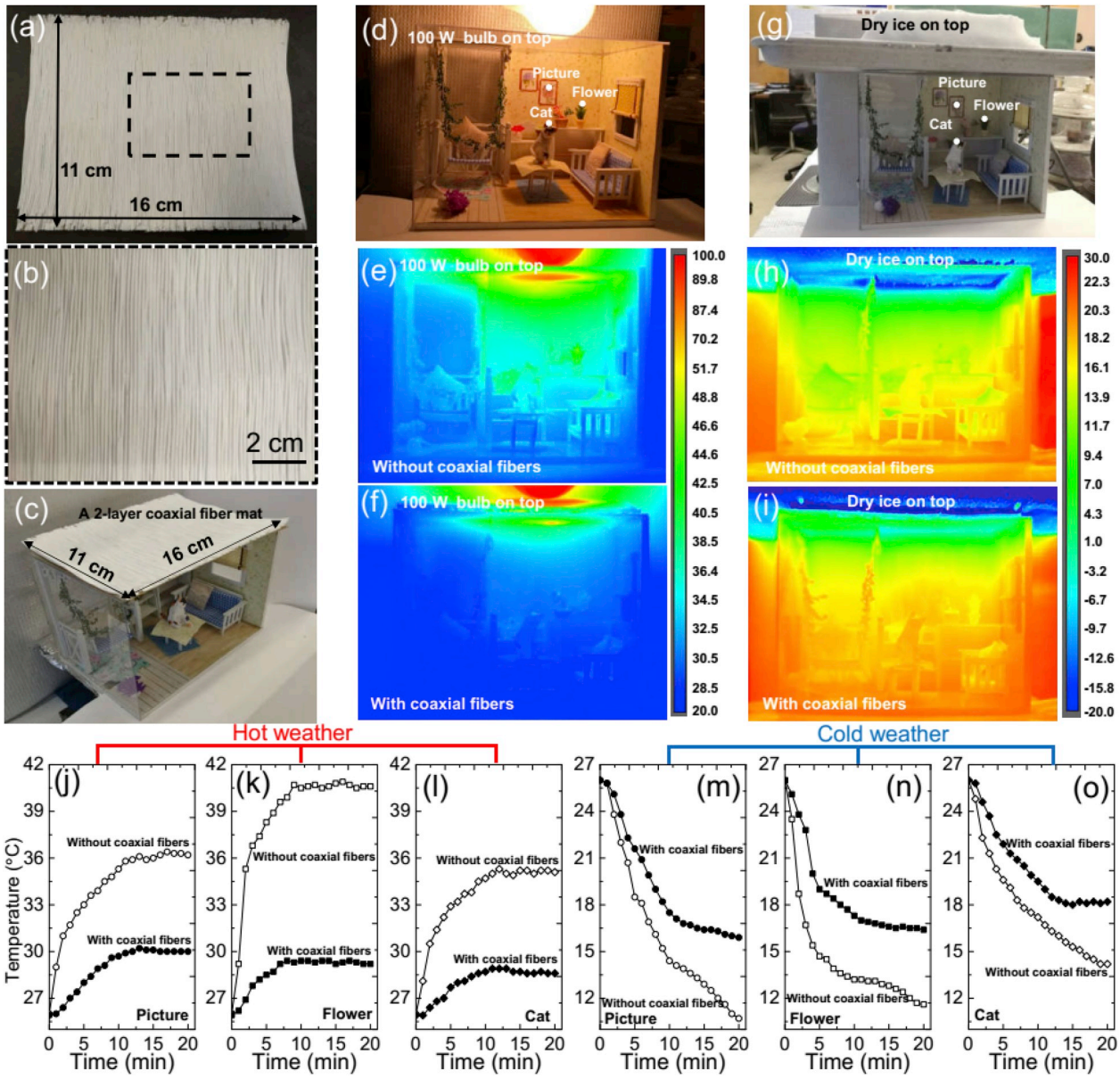

Fig. 5. Demonstration of the thermal insulation application using the coaxial fibers. (a, b) Photographs of a 2-layer coaxial fiber mat in the top view. (c) A toy house (16 cm × 11.5 cm × 13 cm) with the front side open was assembled for the demonstration of the building insulation. The 2-layer coaxial fiber mat was placed on top of the roof. (d) Photograph of the toy house in hot environments. A bright 100 W bulb was placed 1 cm away from the top of the roof or the fiber mat to create the "hot weather" around the toy house. The marked white dots of "Picture", "Flower", and "Cat" are the representative temperature detection locations in the following experiments. (e, f) The thermal images of the toy house in a "hot weather" without and with the coaxial fiber mat on the roof, respectively. (g) Photograph of the toy house in cold environments. A slab of dry ice (16 cm × 12 cm × 3 cm) carried by an aluminum tray was placed at the top create the "cold weather" around the toy house. (h, i) The thermal images of the toy house in a "cold weather" without and with the coaxial fiber mat on the roof, respectively. The thermal images in (e), (f), (h), and (i) were taken after 20 min stabilization. (j–l) display the impact of the coaxial fibers for the temperature change with time of the "Picture", "Flower", and "Cat" (as shown in Fig. 5d), respectively in the "hot weather". (m–o) display the impact of the coaxial fibers for the temperature change with time of the "Picture", "Flower", and "Cat", respectively in the "cold weather."

environmental temperatures from −20 to 150 °C, making it beneficial for civil engineering and related industrial applications.

3. Conclusion

Highly porous and strong coaxial cellulose-rich fibers have been successfully engineered to consist multiscale porous CA/PAA sheath and CNF aerogel core as novel thermal insulation materials. Wet-spun hollow fibers provide the porous sheath to not only facilitate the formation of CNF aerogel in the core but also protect and give mechanical strength to the aerogel core. The coaxial fibers exhibit unique characteristics of high porosity (85%), low density (0.2 g cm^3), and high specific tensile strength (23.5 ± 2.5 MPa g cm^{-3}) to perform effectively as thermal insulators under a wide range of working temperatures from −20 to 150 °C. Both the porous sheath and the CNF aerogel core of the coaxial fibers play crucial roles in achieving the excellent thermal insulation. Most significantly, the structural formation approach for the porous sheath and core coaxial fibers opens up entirely new possibilities in engineering continuous fibrous form of aerogel in varied diameters and is scalable. The development and proof of concept of these porous coaxial fibers represent a breakthrough in biobased thermal insulation materials, and this approach may revolutionize sustainable energy-

saving solution for wearable devices and building structures.

4. Experimental section

Materials: Cellulose acetate (CA-398-30L-HV, $M_n = 50$ k*Da*) was purchased from Eastman Chemical Company. Poly (acrylic acid) (PAA, $M_n = 4{,}000$ k*Da*) was purchased from Sigma Aldrich. Dimethylacetamide (DMAc) was purchased from EMD Chemicals. Cellulose nanofibrils (CNFs) were derived from rice straw cellulose via combined TEMPO-mediated oxidation and mechanical blending, as reported previously [14,16]. Briefly, 1.0 g of rice straw cellulose was oxidized in an aqueous solution containing 0.016 g of TEMPO, 0.1 g of NaBr and 5 mmol NaClO at pH 10.0. After centrifugation and dialysis, the TEMPO-oxidized cellulose was blended (Vitamix 5200, Vita-Mix Corporation) at 37,000 rpm for 30 min, centrifuged (5,000 rpm, 15 min) to collect the supernatant to be concentrated using a rotary evaporator (Buchi Rotavapor R-114) to 0.7 wt% and stored at 4 °C for preparation of aerogel fibers.

Preparation of hollow CA/PAA fibers: PAA (0.2 g) was first vigorously stirred in DMAc (13.1 g) for 1 h, then CA (2.3 g) was added to prepare 16 wt% concentration of 23:2 w/w CA-PAA w/w mixture and stirred for 4 h. Each of the core (water) and shell solutions (CA/PAA in DMAc) was loaded into 10 mL syringes and spun through respective outer (17G) and inner (23G) stainless steel needles at the same 300 μl min^{-1} rate using Fusion 200 syringe pumps (Chemyx Inc.). The fibers were continuously spun into a water bath at ambient temperature and collected on a 50 mm diameter winding spool at 2–4 m min^{-1} line speed. The as-spun wet fibers were soaked in a water bath for 15 h to remove residual DMAc, then frozen (−20 °C, 15 h) and lyophilized (−50 °C, 4 d, Free Zone 1.0L Benchtop Freeze Dry System, Labconco, Kansas City, MO) to yield the hollow fibers.

Preparation of CA/PAA-sheath CNF-aerogel core coaxial fibers: The as-prepared CNF aqueous dispersion at 0.7 wt% was stirred for 10 min and loaded into a 10 mL syringe. The CNF dispersion was then injected into the CA/PAA hollow fibers with lengths up to 8 m using a Fusion 200 syringe pumps (Chemyx Inc.) at 300 μl min^{-1}. The aq. CNF containing CA/PAA hollow fibers were then frozen (−20 °C, 15 h) and lyophilized (−50 °C, 4 d, Free Zone 1.0L Benchtop Freeze Dry System, Labconco, Kansas City, MO) to yield aerogel core coaxial fibers.

Characterization: The height of CNFs was imaged by Atomic force microscopy (AFM). 10 µl CNF suspension (0.0001 wt%) was deposited onto a freshly cleaved mica surface, air-dried, scanned (Asylum-Research MFP-3D) in air under ambient condition using tapping mode with OMCL-AC160TS standard silicon probes. CNFs was imaged by transmission electron microscopy (TEM) on a JEM-1230 electron microscope (JEOL) to determine widths and lengths. CNF suspension (0.0001 wt%) was deposited onto glow-discharged carbon-coated TEM grids (Ted Pella Inc., Redding, CA) with the excess liquid being removed by blotting with a filter paper after 10 min. The specimens were then negatively stained with 2% phosphotungstic acid solution. Scanning electron microscopy (SEM) was performed on the cross section, inner and outer surface of the fibers using a Quattro S machine at high vacuum mode (Thermo Scientific). All samples were sputtered with the gold of 3–5 nm thickness before imaging. The diameter of the microvoids, submicron pores, and nanopores on the inner and outer surface of the CA/PAA sheath were measured and averaged from 30 pores by ImageJ. The cross-section dimension of the fibers was measured from SEM images, and their mass was measured by a balance with 0.1 mg resolution, to calculate the fiber density (ρ_f). The porosity of the fibers (P_f) was calculated as $P_f = 1 - \rho_f/\rho_b$, where ρ_b is the bulk density of cellulose equals 1.3 g cm^{-3}. The mechanical behavior of hollow CA/PAA fiber, CA/PAA-wrapped CNF aerogel fibers was measured by a 5566 Instron universal testing machine at a constant 5% min^{-1} strain rate. Fiber samples in 3 cm length, were coated with epoxy adhesive at each end to protect them from damage during clamping. The tensile strength, Young's modulus, and elongation were collected from at least 10 samples for each formulation, and their average values and standard deviation are reported. As it is difficult to directly measure the thermal conductivity of a single fiber, we prepared a representative sample containing 4 layers of tightly packed fibers; each layer contains 10 unidirectional fibers. The thermal conductivities of the samples were estimated by measuring layered fiber arrays using a Transient Hot Disk TPS 2500 S meter. For comparison, a CNF aerogel sample (diameter 11 cm, thickness: 1 mm) was also prepared and thermal conductivity was measured by the same meter. Thermal images of the fibers were taken using an A320 thermographic camera (FLIR Systems, Inc.) at a frame rate of 10 Hz. The working distance between the camera lens and the sample is approximately 22 cm. The representative sample is constructed containing layers of tightly packed fibers; each layer contains 10 unidirectional fibers. The fiber length of interest is 2.5 cm. During the measurements, the ambient temperature is around 26 °C. The thermal images were taken when the fiber surface temperature was stable.

Declaration of competing interest

The authors declare no conflict of interest.

Acknowledgements

The authors appreciate the funding support from the California Rice Research Board.

Appendix A. Supplementary data

Supplementary data to this article can be found online at https://doi.org/10.1016/j.nanoen.2019.104305.

References

[1] a) F. Qian, P.C. Lan, M.C. Freyman, W. Chen, T. Kou, T.Y. Olson, C. Zhu, M. A. Worsle, E.B. Duoss, C.M. Spadaccini, T. Bauman, T.Y.J. Han, Nano Lett. 12 (2017) 7171;
b) S. Araby, A.D. Qiu, R.Y. Wang, Z.H. Zhao, C.H. Wang, J. Ma, J. Mater. Sci. 51 (2016) 9157.
[2] a) X. Zhou, W. Yao, W. Gao, H. Chen, C. Gao, Adv. Mater. 29 (2017), 1701482;
b) S. Chandrasekaran, P.G. Campbell, T.F. Baumann, M.A. Worsley, J. Mater. Res. 32 (2017) 4166.
[3] a) X. Zhang, J. Liu, B. Xu, Y. Su, Y. Luo, Carbon 29 (2011) 1884;
b) M. Kotal, J. Kim, J. Oh, I.K. Oh, Front. Mater. (2016) 3, https://doi.org/10.3389/fmats.2016.00029.
[4] a) A. Lamy-Mendes, R.F. Silva, L. Duraes, J. Mater. Chem. A 6 (2018) 1340;
b) Y. Kobayashi, T. Saito, A. Isogai, Angew. Chem. Int. Ed. 53 (2014) 10394;
c) K. Sakia, Y. Kobayashi, T. Saito, A. Isogai, Sci. Rep. 6 (2016) 20434;
d) S.-L. Li, B.-C. Hu, Y.-W. Ding, H.-W. Liang, C. Li, Z.-Y. Yu, Z.-Y. Wu, W.-S. Chen, S.-H. Yu, Angew. Chem. Int. Ed. 57 (2018) 7085.
[5] a) K.H. Kim, M. Vural, M.F. Islam, Adv. Mater. 23 (2011) 2865;
b) C. Ziegler, A. Wolf, W. Liu, A.K. Herrmann, N. Gaponik, A. Eychmuller, Angew. Chem. Int. Ed. 56 (2017) 13200;
c) B. Cai, R. Hübner, K. Sasaki, Y. Zhang, D. Su, C. Ziegler, M.B. Vukmirovic, B. Rellinghaus, R.R. Adzic, A. Eychmüller, Angew. Chem. Int. Ed. 57 (2018) 2963.
[6] I. Smirnova, P. Gurikov, J. Supercrit. Fluids 134 (2018) 228.
[7] A. Du, B. Zhou, Z.H. Zhang, J. Shen, Materials 6 (2013) 941.
[8] M. Venkataraman, R. Mishra, T.M. Kotresh, J. Militky, H. Jamshaid, Text. Prog. 48 (2016) 55.
[9] Z. Xu, Y. Zhang, P.G. Li, C. Gao, ACS Nano 6 (2012) 7103.
[10] I. Karadagli, B. Schulz, M. Schestakow, B. Milow, T. Gries, L. Ratke, J. Supercrit. Fluids 106 (2015) 105.
[11] B. Schulz, T. Meinert, D. Bierbusse, M. Busen, N. Kortzinger, M. Stankowski, G. Seide, Chem. Ing. Tech. 88 (2016) 1501.
[12] F. Jiang, Y.L. Hsieh, ACS Omega 3 (2018) 3530.
[13] J. Zhou, Y.L. Hsieh, ACS Appl. Mater. Interfaces 10 (2018) 27902.
[14] F. Jiang, Y.L. Hsieh, J. Mater. Chem. A 2 (2014) 6337.
[15] F. Jiang, Y.L. Hsieh, J. Mater. Chem. A 2 (2014) 350.
[16] F. Jiang, Y.L. Hsieh, Carbohydr. Polym. 95 (2013) 32.
[17] F. Jiang, Y.L. Hsieh, ACS Appl. Mater. Interfaces 9 (2017) 2825.
[18] N. Lavoine, L. Bergstrom, J. Mater. Chem. A 5 (2017) 16105.
[19] X. Du, Z. Zhang, W. Liu, Y.L. Deng, Nano Energy 35 (2017) 299.
[20] F. Jiang, S. Hu, Y.L. Hsieh, ACS. Appl. Nano. Mater. 1 (12) (2018) 6701.
[21] a) N. Peng, N. Widjojo, P. Sukitpaneenit, M.M. Teoh, G.G. Lipscomb, T.S. Chung, Prog. Polym. Sci. 37 (2012) 1401;
b) J.C. Su, Q. Yang, J.F. Teo, T.S. Chung, J. Membr. Sci. 355 (2010) 36.
[22] O.J. Lee, K.H. Lee, T.J. Yim, S.Y. Kim, J. Non-Cryst. Solids 298 (2002) 287.
[23] Y. Cui, H.X. Gong, Y.J. Wang, D.W. Li, H. Bai, Adv. Mater. 30 (2018), 1706807.

[24] T.W. Cheung, L. Li, Text. Res. J. (2017), https://doi.org/10.1177/0040517517741164.
[25] D. Illera, J. Mesa, H. Gomez, H. Maury, Coatings 8 (2018) 345.
[26] K. Uetani, K. Hatori, Sci. Technol. Adv. Mater. 18 (2017) 877.
[27] Y. Yang, Physical Properties of Polymer Handbook, Springer, New York, NY, 2007, pp. P155–P163.
[28] C. Rudaz, R. Courson, L. Bonnet, S. Calas-Etienne, H. Sallée, T. Budtova, Biomacromolecules 15 (6) (2014) 2188–2195.